Appendix B

With kind permission from Springer Science+Business Media:

Experimental Mechanics, Three-Dimensional Full-Field Measurements of Large Deformations in Soft Materials using Confocal Microscopy and Digital Volume Correlation, 47(3), 2007, p. 427-438, Franck, C., Hong, S., Maskarinec, S.A., Tirrell, D.A., and G. Ravichandran, Figures 1–12.

Abstract

A three-dimensional (3-D) full-field measurement technique was developed for measuring large deformations in optically transparent soft materials. The technique utilizes a digital volume correlation (DVC) algorithm to track motions of subvolumes within 3-D images obtained using fluorescence confocal microscopy. In order to extend the strain measurement capability to the large deformation regime (> 5%), a stretch-correlation algorithm was developed and implemented into the Fast Fourier Transform (FFT)-based DVC algorithm. The stretch-correlation algorithm uses a logarithmic coordinate transformation to convert the stretch-correlation problem into a translational correlation problem under the assumption of small rotation and shear. Estimates of the measurement precision are provided by stationary and translation tests. The proposed measurement technique was used to measure large deformations in a transparent agarose gel sample embedded with fluorescent particles under uniaxial compression. The technique was also employed to measure non-uniform deformation fields near a hard spherical inclusion under far-field uniaxial compression. Introduction of the stretch-correlation algorithm greatly improved the strain measurement accuracy by providing better precision especially under large deformation. Also, the deconvolution of confocal images improved the accuracy of the measurement in the direction of the optical axis. These results shows that the proposed technique is well-suited for investigating cell-matrix mechanical interactions as well as for obtaining local constitutive properties of soft biological tissues in 3-D.

B.1 Introduction

The importance of mechanical signals in directing cellular behaviors such as adhesion, motility, differentiation and morphogenesis has become evident in recent years [1-4]. Yet there is minimal understanding regarding the intricate coupling of mechanical and biochemical signaling at the cellular level [5]. This knowledge gap is mainly due to the lack of experimental tools that can accurately measure forces and deformations at the cellular or sub-cellular level with sufficiently high sensitivities and wide applicable ranges. Previous investigations on the influence of mechanical stimuli predominantly focused on two-dimensional cell-substrate interactions that occur during cell spreading and migration [6, 7]. Although these reports have contributed much to the understanding of cell behavior in two-dimensional environments, it has been recently demonstrated that cells show distinct three-dimensional morphologies and interactions, as expected in vivo [8-10]. Thus, in order to characterize and understand cell-matrix interactions at the single cell and sub-cellular level, forces and motions in three-dimensions must be quantitatively measured and analyzed. Even though technical advances in microscopy have allowed for feature sizes as small as nanometers to be resolved [11], the nature of most of the previously presented measurements remains two-dimensional. Attempts to employ stereo-imaging techniques to capture three-dimensional deformation fields [12] have been successful, but these methods only provide surface information.

Motivated by the need for capturing mechanical responses of a motile cell in a three-dimensional extracellular matrix (ECM), a promising new technique that uses the three-dimensional imaging capability of confocal microscopy coupled with a digital volume correlation (DVC) algorithm was developed in this study. Analogous to the

digital image correlation (DIC) technique [13, 14] where in general two-dimensional displacement fields are measured, the DVC uses volume subsets to track the three-dimensional displacement fields within the matrix. One main advantage of the proposed algorithm over those reported previously [15-17] is that the method presented here takes into consideration the stretch deformation of each volume subset. Also, a deconvolution algorithm is used to minimize the blurring of the confocal images. These two improvements allow for a more accurate strain estimate, especially when local strains are large and subset deformation is significant. Another advantage over previous studies is that the results do not depend on the local sample feature size to achieve high correlation resolution, but rather can be tailored to the relevant length scale of interest. This is achieved by utilizing commercially available fluorescent markers rather than relying on the autofluorescence of the sample, which can limit the field of view. The method presented here allows the user to choose virtually any field of view provided the availability of the appropriate markers. Using this method, material properties of soft materials can be experimentally determined, especially where conventional characterization techniques fail due to the compliant nature of the material.

This paper is organized as follows. In Section B-2, a brief description of the laser scanning confocal microscope (LCSM) is presented. The details of the digital volume correlation methodology and algorithm developments are described in Section B-3. The experimental procedures are given in Section B-4 and the results are presented and discussed in Section B-5. Conclusions for the present study are summarized in Section B-6.

B.2 Laser Scanning Confocal Microscope (LSCM)

Confocal microscopy has emerged as a powerful imaging technique owing to the optical sectioning capability enabling construction of three-dimensional images. In conventional wide-field microscopy, light is collected from the entire sample volume, including the focal plane as well as all other planes, whereas, in confocal microscopy, light is generally collected from the focal plane only. This is achieved by using a pinhole in front of a photomultiplier tube (PMT) detector that blocks the incoming light from all other planes. As illustrated in Figure B-1, the solid line represents light reflected or emitted from the focal plane, while the dashed line represents light from the out-of-focus plane. The overall contrast and resolution of the image is significantly increased as compared to conventional wide-field microscopy where the image is blurred by out-of-plane light. Furthermore, the inherent optical sectioning of the specimen in confocal microscopy allows the assembly of three-dimensional image volumes by stacking together individually acquired planar slices. In a LSCM system, a laser with a single-diffraction limited spot size is used to sequentially scan a selected focal plane. Thus, the image is not formed using a CCD camera as in conventional microscopy, but rather the image is a result of the light's interaction with successive areas of the specimen, i.e. the image is recorded pixel by pixel analogous to a scanning electron microscope. The resulting image is generally superior in resolution to images recorded by conventional optical microscopy. A more detailed description of the confocal principle and the current applications of confocal microscopy are well documented and can be found elsewhere [18, 19].

In the present study, fluorescent markers were added to the transparent materials of interest and they served as image sources for constructing the 3-dimensional images and as markers for performing DVC described in the next section.

B.3 Digital Volume Correlation (DVC)

B.3.1 Principle of DVC

LSCM provides discretized volume images visualizing 3-dimensional structural patterns of fluorescent markers in a transparent sample. In this study, the combination of digital volume correlation (DVC) and confocal images is used to achieve 3-dimensional full-field deformation measurements as an extension of the vision-based surface deformation measurement techniques, well-known as digital image correlation (DIC). The basic principle of the DVC is schematically illustrated in Figure B-2. Two confocal volume images of an agarose gel with randomly dispersed fluorescent particles are obtained before and after mechanical loading. Then, the two images are subdivided into a set of subvolumes that are centered on the points of interest. Using each pair of corresponding subvolume images, the respective local displacement vector can be obtained from 3-dimensional volume correlation methods.

Consider two scalar signals $f(x)$ and $g(x)$ which represent a pair of intensity patterns in a sub-volume Ω before and after a continuous mapping, $\hat{y}(x): x \rightarrow y$, respectively. Assuming that the signal is locally invariant during the mapping, $f(x) = g(y(x))$, subvolume-wise correlation matching can be obtained by finding an optimal mapping that maximizes the cross-correlation functional defined as

$$m(\hat{y}) = \int f(x)g(y(x))d\Omega_x \tag{1}$$

The methodology is illustrated using a translational volume correlation, which is presented below. The continuous mapping is assumed to be a rigid translation, $y = x + c$, and the cross-correlation function is represented as a function of a displacement vector c as

$$m(c) = \int f(x)g(x+c)d\Omega_x \tag{2}$$

The cross-correlation function can be written using Fourier transforms as follows

$$m(c) = F^{-1}\left[F\left[f(x)\right]^* F\left[g(x)\right]\right] \tag{3}$$

where the Fourier transform of $f(x)$ is defined as

$$F\left[f(x)\right] = \int f(x)e^{-ik\bullet x}d\Omega_x \tag{4}$$

and * denotes the complex conjugate. The discrete cross-correlation function can be computed efficiently by using the Fast Fourier Transform (FFT) algorithm. Then, the rigid translation vector **c** can be estimated from the location of the cross-correlation peak with respect to the origin. Finding a voxel-resolution displacement vector **c** from the discrete cross-correlation function is straightforward and provides half-voxel accuracy. Determining the displacement vector **c** in sub-voxel accuracy generally requires fitting and interpolation of the correlation function near the peak. Various fitting models have been used in the past [20, 21], employing somewhat arbitrary assumptions that the cross-correlation function near the peak can be approximated by a Gaussian or a parabolic function. The sub-voxel accuracy of such peak-finding algorithms is determined by the choice of fitting function as well as the size of the fitting window. In this study, a three-dimensional quadratic polynomial fitting is used to accurately fit the correlation function near the peak and hence provide improved sub-pixel accuracy.

However, significant measurement error can be introduced from the decorrelation of the intensity patterns when the rotation or the stretch of the subvolume is large. Thus, applications of such simple correlation algorithms have been limited to small strain and small rotation problems due to the inherent limitation of the rigid-translation assumption. In general, the applicability of such algorithm is limited up to about 5% of strain or 0.05 radian of rotation angle [20]. In order to overcome this limitation and to obtain more accurate displacement measurements, a higher-order approximation of the deformation field within each subvolume is required for large deformation measurements in soft materials. In the following section, an extension of the FFT-based DVC to measure large deformation fields is presented.

B.3.2 Stretch correlation

Assuming uniform deformation of each subvolume, a general homogeneous deformation field can be written as

$$\hat{y}(x) = Fx + c \tag{5}$$

with a deformation gradient tensor $F = I + u\nabla$ and a displacement vector u. Therefore, any uniform deformation in 3-dimensions can be represented with a total of 12 parameters which consist of 3 displacement components and 9 displacement gradient components. Optimal programming in 3-dimensions for a total of 12 degrees of freedom (DOF) is computationally expensive in conventional correlation algorithms.

Alternatively, the general homogeneous deformation can be represented with a polar decomposition of the deformation gradient tensor as

$$\hat{y}(x) = RUx + c \tag{6}$$

where R is the orthogonal rotation tensor and U is the symmetric right-stretch tensor. Then, the general homogeneous deformation in 3-dimensions is represented with 6 stretch, 3 rotation and 3 translation components. Depending on the dominant mode of the deformation of interest, the correlation algorithm can be modified to include additional optimization parameters selectively. A digital volume correlation algorithm that includes three rotational degrees of freedom has been presented previously [17]. In this study, assuming small rotations and small shear stretch components, three normal stretch components are included as additional correlation parameters in the FFT-based DVC algorithm, as an extension of the stretch-correlation algorithm developed for large deformation measurements in two-dimensions [22].

Neglecting the small rotations, the mapping of a pure homogeneous deformation and a rigid translation is written as

$$\hat{y}(x) = Ux + c \tag{7}$$

When the loading axes are aligned with the global coordinate axes so that the shear stretch components are small, the invariant condition can be written as

$$f(x) \approx g(\overline{U}x + c) \tag{8}$$

where U denotes the diagonal part of U. Then, the six optimization parameters for the stretch correlation in DVC algorithm are $\{c_1, c_2, c_3, U_{11}, U_{22}, U_{33}\}$.

In the case of a pure stretch problem without any translation, a simple coordinate transform into a logarithmic scale converts the stretch correlation problem into a simple translational correlation problem. However, when there is a non-zero translation, the coordinate transform cannot be directly performed in the spatial-domain to achieve the

stretch correlation. Therefore, an equivalent invariant condition of (8) in the Fourier-domain is considered to implement the stretch correlation in the Fourier-domain as

$$\left\|\overline{U}\right\|F(\overline{U}k) = e^{ik\bullet c}G(k) \tag{9}$$

where $F(k)$ and $G(k)$ represent Fourier transforms of $f(x)$ and $g(x)$, respectively. Then by using the Fourier power spectrums only and therefore dropping the phase term, a translation-invariant stretch-correlation problem can be achieved in the Fourier-domain. A stretch cross-correlation function to be maximized for determining the 3 axial stretch components neglecting the determinant of jacobian is shown as

$$m(\overline{U}) = \int \left|F(\overline{U}k)\right\|G(k)\left|d\Omega_k\right. \tag{10}$$

The stretch correlation problem in the Fourier-domain can be transformed into a translational correlation problem in a log-frequency domain as

$$\tilde{m}(\eta) = \int \left|\tilde{F}(\xi+\eta)\right\|\tilde{G}(\xi)\left|d\Omega_\xi\right. \tag{11}$$

where $\xi = \log_b k$ and $\eta = \log_b \overline{U}$. The translational correlation problem in the log-frequency domain can be easily solved using (3). Finally, the three axial stretch components can be obtained from the optimal vector η in the log-frequency domain as follows

$$U_{11} = b^{\eta_1}, U_{22} = b^{\eta_2}, U_{33} = b^{\eta_3} \tag{12}$$

The accuracy of the obtained stretch components depends strongly on the spectral content of the original signals. If the signals are already band-limited, special considerations, such as normalizing the power spectrums and employing the Hanning window, must be included to achieve robust stretch correlations. Also, in the numerical implementation of the stretch correlation algorithm, incorporating zero-padding of the signals before Fourier transforms can improve the overall accuracy of the stretch

correlation algorithm by providing ideal interpolations of the Fourier transforms at a cost of increased computational load.

In Figure B-3, the stretch-correlation procedures are illustrated using a one-dimensional example. Two reference and deformed signals representing 10% of uniform strain are shown in Figure B-3(a). The Fourier power spectrums of the two signals are shown in Figure B-3(b). Note that only half of the full frequency range is shown due to the inherent Fourier symmetry. In Figure B-3(c), the equivalent Fourier power spectrums are shown after the zero-padding as ideal interpolations of the power spectrums in Figure B-3(b). Figure B-3(d) shows the Fourier power spectrums along the logarithmic axis. After interpolating the power spectrums using a uniform interval in the log-frequency domain as shown in Figure B-3(e), the translational correlation as presented in (11) can be applied to find the 1-D stretch value. Extension of the 1-D stretch-correlation into 2-D or 3-D is straightforward as long as rotation and shear stretch are small.

In the implementation of 3-D stretch correlation, 2-D projections of the 3-D subvolume images were used to circumvent the geometrically increased computational load after the zero padding, as shown in Figure B-4. Essentially, the stretch correlations using the large zero-padding were conducted in a reduced dimension for computational efficiency. Three separate 2-D projections were conducted so that three sets of two stretch components can be obtained. From the six stretch values, three stretch components (U_{11}, U_{22}, U_{33}) were obtained by computing the average of the two corresponding stretch components.

Once the three axial stretch components are found, the translation vector **c** can be determined more accurately by conducting the stretch-compensated translational correlation using

$$m(c) = \int \tilde{f}(x')g(x'+c)d\Omega_{x'} \tag{13}$$

where $f(x) = \tilde{f}(\overline{U}x)$ and $x' = \overline{U}x$. The stretch-compensated translational correlation requires the initial subvolume image $f(x)$ to be stretched to $\tilde{f}(x')$ according to the obtained three stretch values. Therefore the process involves sub-voxel interpolations of the initial subvolume image. Because the stretch part of the deformation is compensated, a more accurate translation vector **c** can be obtained. The stretch correlation and the translational correlation were conducted iteratively to achieve converging results. For all experiments executing the stretch and translational correlation twice yielded sufficient convergence based on a mean difference criterion, where the mean and standard deviation of the difference of the before and after displacement matrices were compared (this is similar to least-square error estimate). Such an iteration process is equivalent to the iterative optimization of a correlation coefficient in conventional image correlation scheme conducted in the spatial domain.

Finally, the displacement gradients were computed by using a 3-dimensional least-square fitting of each displacement component in a 3x3x3 grid of neighboring data points. Although more sophisticated smoothing or filtering algorithm can be employed before or during the gradient calculation in order to obtain smoother strain fields, no such algorithm was used in this study to assess the performance and robustness of the proposed DVC algorithm. Once the displacement gradient fields are determined, either

infinitesimal or finite strain values can be computed from the displacement gradient fields.

B.3.3 DVC using confocal microscope images

The spatial resolution of a confocal microscope is determined by the 3-dimensional point spread function (PSF) which is an intensity distribution near the focal point corresponding to a volume image of a point light source under a diffraction-limited imaging system. The 3-dimensional PSF has an ellipsoidal shape elongated along the optical axis [23, 24]. Thus, the obtained confocal image is the convolution of actual intensity distributions using the PSF as a kernel. Consequently, the axial spatial resolution of confocal imaging is 3 to 10 times worse than the lateral spatial resolution depending on the refractive index of the medium and the numerical aperture of the objective lens.

In Figure B-6 (a), an isosurface plot of a typical confocal subvolume image (64x64x64 voxels) of a transparent agarose gel with randomly dispersed fluorescent spherical particles of 2 voxels diameter is shown. The spherical fluorescent particles appear as axially elongated ellipsoids. The blurring in the axial direction causes increased uncertainties in the DVC measurements of the axial direction components. The consequence of such blurring is particularly critical to the performance of the stretch correlation algorithm that uses the Fourier power spectrums. In this study, the noise-resistant Lucy-Richardson deconvolution algorithm [25] was used to deconvolve the raw confocal images using a sinc PSF in the axial direction prior to the stretch correlation. Figure B-6 (b) shows a subvolume image obtained after deconvolution of the raw image.

There are two additional confocal-imaging artifacts caused by the refractive index mismatch in the optical path. First, spherical aberration due to the refractive index mismatch causes asymmetric distortions of the 3-dimensional PSF as a function of the penetration depth. Such a distorted and depth-dependent PSF makes the deconvolution of the confocal images difficult and causes significant error in the DVC. Effects of such spherical aberration in confocal imaging have been extensively studied in the past [26, 27]. In practice, the spherical aberration can be minimized by adjusting the correction collar commonly equipped in commercial microscope objectives. In order to minimize the distortion of the PSF within the field of view, the correction collar needs to be adjusted appropriately prior to each test. The second form of confocal imaging artifact due to the refractive index mismatch is caused by the fact that the focal point does not follow the axial motion of the scanning stage [28, 29]. This causes an over- or under-estimation of the depths depending on the ratio of the refractive index mismatch. This apparent discrepancy between the axial and the lateral scanning resolutions can be calibrated by imaging large fluorescent microspheres embedded in a sample.

B.4 Experimental Procedures

Test specimens were prepared from a 1% (w/v) solution of agarose (J.T. Baker, NJ) in standard 0.5X TBE buffer (Tris/Borate/EDTA, pH 8.0). The agarose solution was heated until molten, and carboxylate-modified red fluorescent (580/605) polystyrene microspheres (Invitrogen, CA) of 1μm diameter were injected into the liquid agarose. The nominal volume fraction of fluorescent markers in the gel was 0.3%. The addition of the fluorescent microspheres seemed negligible to both the local or global mechanical

response of the agarose gel. The nominal volume fraction of fluorescent markers in the gel was 0.3%. The mixture was cast into a pre-chilled Teflon mold mounted onto a glass plate. Samples were left at room temperature for 5 minutes to solidify. This protocol yielded circular agarose specimens with typical dimensions of 6.4 mm diameter and 1.4 mm height. For spherical inclusion experiments, spherical polymethylmethacrylate (PMMA) beads (Sigma-Aldrich, MO) of 100 μm diameter were added to the mixture before casting.

In order to apply uniaxial compressive loading to the sample while imaging, a miniature loading-fixture was built and mounted directly on top of the microscope stage of an inverted optical microscope as shown in Figure B-7. The sample was kept immersed in the buffer solution to prevent swelling or shrinking during the test. The compressive loading was achieved by translating a micrometer head with a resolution of 1 μm. For all experiments the imposed strain increments were controlled by the micrometer and were calculated using the dimension of the specimen and the imposed loading (displacement) step. The resulting applied force was measured using a 10-gram load cell (A.L. Design, NY). Nominal stress-strain curves were compiled using this setup for each test. The LSCM used in this study was a confocal system (Nikon C-1) combined with an inverted optical microscope (Nikon TE-2000-U). A 40x CFI planar fluor air objective with a numerical aperture of 0.6 was used in all experiments.

B.5 Results and Discussions

B.5.1 Characterization of measurement precision

In order to verify the measurement precision of the DVC algorithm using confocal volume images, two tests were conducted under zero-strain condition. In the first test, two confocal volume images were repeatedly acquired from a stationary sample under zero load. The scanning resolution was 512x512x512 voxels, and the scan spacing was 0.45 μm in all three directions. This resulted in a field of view of 230x230x230 μm^3. In the second test, two confocal images were acquired before and after translating the unloaded sample using the x_3-directional scanning stage of the confocal microscope. The two pairs of the confocal images were analyzed by using the DVC algorithm with a subvolume size of 64x64x64 voxels. Displacements were measured at 15x15x15 points (total 3375 points) in a uniform grid of 32 voxels spacing. Displacement gradients were then calculated by using the displacement data at 3x3x3 neighboring grid points following linear least-square fitting of the displacement components. Although the quadratic (Lagrangian) or the logarithmic (true) strain measure can be used for large deformation analysis, the linear (engineering) strain measure was used to represent the deformations in this study. As a quantitative measure of the uncertainties in the DVC results, standard deviation values of three displacement components and three normal strain components were computed and summarized in Table B-1.

The absolute values of the uncertainties in the displacements and the strains are comparable to previously reported results [15, 16]. These measurement uncertainties are likely due to the noises in the confocal images caused by the PMT detector noise as well as the positional uncertainty of the laser scanning system. It is also noted that the axial

uncertainties of the displacement and strain components in the x_3-direction are approximately 3 to 5 times higher than the corresponding lateral uncertainties in the x_1- and x_2-directions (in-plane). This result shows that the axially elongated three dimensional PSF causes a significantly degraded measurement precision in the x_3-direction. These tests under zero-strain condition provide a simple way to assess baseline uncertainties of the measurements using the DVC algorithm.

B.5.2 Uniaxial compression test

In order to verify the 3-dimensional deformation measurement capability of the DVC using the LSCM, the agarose gel sample was compressed uniaxially with nominal strain increments of 2-3%. The total imposed nominal strain was approximately 10%. The obtained confocal images were analyzed using the DVC algorithm with a subvolume size of 64x64x64 voxels. Figure B-8 (a) shows a vector plot of the measured displacement field. Figure B-8 (b) shows a 3-dimensional contour plot of the vertical displacement components.

In order to assess the performance of the DVC algorithm with the stretch-correlation for large deformation measurements, accuracy and precision must be established systematically. The accuracy and the precision of a measurement technique are usually achieved by repeatedly measuring some traceable reference standard. Then, the accuracy and precision are typically quantified as the difference between the mean of the measured values and the true value, and as the standard deviation of the measured values, respectively.

Mean and standard deviation values of the measured strain fields are presented in Table B-2 to assess the effectiveness of the stretch-correlation algorithm. The mean values of the lateral strain components ε_{11} and ε_{22} are close to zero and smaller than their corresponding standard deviation values, i.e. the measurement precision, and are therefore negligible. The standard deviations of the no-stretch-correlated and stretch correlated lateral strain components are similar illustrating that the stretch-correlation does not improve the precision of the strain measurements for small strains. Comparing the no-stretch and stretch-corrected axial strain component ε_{33}, the difference of 0.09% between the two mean values is smaller than their corresponding standard deviation values, which shows that the stretch correlation does not improve the accuracy of the *average* strain measurement. However, the standard deviation in the stretch-correlation case is less than half of that in the no stretch-correlation case. This proves that the stretch correlation greatly improves the precision of the large-deformation measurement. Although precise measurements do not necessarily mean accurate measurements, it is often not possible to reliably achieve high accuracy in individual measurements without precision. This point is particularly important in the full-field measurement of non-uniform deformation fields.

Since it is not possible to know the true value of the compressive strain up to the level of accuracy and precision of the measurement technique under investigation, the absolute accuracy of the proposed DVC method cannot be assessed with the nominal strain value from the global measurement. However it is clear that overall measurement accuracy can be improved by providing better precision, since precision is a limit of accuracy. The results from the uniaxial compression test show that the proposed stretch-

correlation algorithm in conjunction with the deconvolution algorithm improved the overall accuracy of large deformation measurement with better precision.

The average axial compressive strain value was 9.3%, whereas the average lateral strain values were negligible. The result showed that the lateral expansion due to the Poisson effect was effectively constrained due to the disc-shaped geometry of the sample. To determine the material properties of the agarose sample correctly the uniaxial test results need to be interpreted as a constrained compression of a soft layer yielding expression (14), where the axial stress-strain ratio for constrained compression is defined as a constrained modulus and related to elastic properties as follows,

$$\frac{\sigma_{33}}{\varepsilon_{33}} = \frac{(1-\nu)E}{(1+\nu)(1-2\nu)}, \ (\varepsilon_{11} = \varepsilon_{22} = 0) \quad (14)$$

where E and ν denote Young's modulus and Poisson's ratio, respectively.

B.5.3 Spherical inclusion problem

In order to demonstrate the capability of the measurement technique using the DVC and the LSCM, a non-uniform 3-dimensional deformation field near a hard spherical inclusion was measured under far-field uniaxial compressive loading. Confocal images near a 100 μm-diameter PMMA bead embedded within the agarose gel sample were recorded during incremental compressive loading. The nominal strain increment was approximately 3%. The scanning resolution was 512x512x512 voxels, and the scan spacing was 0.45 μm in all three directions. The confocal scanning volume near the embedded PMMA bead is illustrated in Figure B-9. Figure B-11 shows a vertical slice of the confocal image along the meridian plane of the PMMA bead at the undeformed configuration. The superimposed uniform grid of 16-voxels spacing represents the

locations where displacements measurements were conducted. The confocal images were analyzed by using the proposed DVC algorithm with a subvolume size of 64x64x64 voxels. The contour maps in Figure B-13 represent constant contours of the horizontal (u_1) and the vertical (u_3) displacement components on the meridian plane. As expected, the dominant mode of the deformation was a constrained uniaxial compression along the x_3-direction. The local distortion of the displacement contours near the PMMA bead indicated that the proposed DVC algorithm effectively captured non-uniform deformation fields near the spherical inclusion.

The experimentally measured displacement fields in Figure B-13 were compared to the analytical solution of the equivalent linear-elasticity problem. Most analytical elasticity solutions of the inclusion problem assume the continuity of displacement at the interface. Considering the high water content in the agarose gel and the large deformations in the sample, the perfect bonding condition is inadequate to accurately represent the present experiment. Using the solution of the sliding inclusion problem under uniaxial loading [30], the analytical solution of the sliding inclusion problem under the laterally-constrained uniaxial compressive loading was constructed by the superposition of three mutually-orthogonal uniaxial compression solutions as shown in Figure B-9. The contour maps in Figure B-15 show the horizontal and the vertical displacement fields of the constructed analytical solution. Qualitative comparisons of the contour maps in Figure B-13 and Figure B-15 indicate that the proposed DVC algorithm was well-suited for the full-field measurements of non-uniform deformation fields in three dimensions. It can be observed that the resolution of the lateral displacement field is

superior to the resolution in the vertical displacement, which is due to the blurring effect caused by the PSF along the optical axis (vertical direction).

A contour map of ε_{33} strain components near the inclusion is shown in Figure B-16 (a). At the bottom of the inclusion, a region of high strain concentration of up to 25% strain was visualized. Figure B-16 (b) displays the line-profile of the ε_{33} strain component along the central axis in x_3-direction. The local compressive strain reaches the far field applied strain level at approximately one radius length away from the center of the bead. The high strain gradient will decrease the accuracy of the stretch-correlation by violating the assumption of uniform stretch deformation. In such cases, iterative applications of the DVC using a smaller subvolume will increase the accuracy of the measurements since each subvolume will be subjected to a more uniform stretch.

B.6 Conclusions

A novel experimental technique for measuring 3-dimensional large-deformation fields in soft materials has been developed. The technique utilizes the 3-dimensional measurement capability of the DVC algorithm in conjunction with the 3-dimensional imaging capability of confocal microscopy. Introduction of the stretch-correlation algorithm and the deconvolution algorithm greatly improved the strain measurement accuracy by providing better precision especially under large deformation. Also, the large-deformation measurement capability of the proposed DVC algorithm was successfully demonstrated by measuring a uniform deformation field for the case of simple uniaxial compression and a non-uniform deformation field surrounding the hard spherical inclusion. This new technique should prove itself particularly useful in

situations where local three dimensional strain non-uniformities need to be measured with high resolution It is expected that the newly developed DVC technique will play a major role in characterizing time dependent cell interactions with its surrounding extracellular matrix including artificially engineered proteins [31], in three dimensions, which will provide valuable insights into the role of mechanical forces on biological processes.

B.7 Acknowledgements

We acknowledge the support provided by the National Science Foundation (DMR # 0520565) through the Center for Science and Engineering of Materials (CSEM) at the California Institute of Technology. GR acknowledges the support of the Army Research Office for providing the DURIP funds for the acquisition of the confocal microscope used in this study. GR gratefully acknowledges the Ronald and Maxine Linde Venture Fund that enabled the acquisition of instrumentation used in this investigation. We would like to thank Mr. Petros Arakelian for his valuable help with the experimental setup.

B.8 References

1. Ingber DE, Dike L, Hansen L, Karp S, Liley H, Maniotis A, McNamee H, Mooney D, Plopper G, Sims J, Wang N (1994) Cellular Tensegrity - Exploring How Mechanical Changes in the Cytoskeleton Regulate Cell-Growth, Migration, and Tissue Pattern During Morphogenesis. International Review of Cytology - a Survey of Cell Biology 150: 173-224.

2. Lo CM, Wang HB, Dembo M, Wang YL (2000) Cell movement is guided by the rigidity of the substrate. Biophysical Journal 79(1): 144-152.

3. Petronis S, Gold J, Kasemo B (2003) Microfabricated force-sensitive elastic substrates for investigation of mechanical cell-substrate interactions. Journal of Micromechanics and Microengineering 13(6): 900-913.

4. Wong JY, Velasco A, Rajagopalan P, Pham Q (2003) Directed movement of vascular smooth muscle cells on gradient-compliant hydrogels. Langmuir 19(5): 1908-1913.

5. Tan JL, Tien J, Pirone DM, Gray DS, Bhadriraju K, Chen CS (2003) Cells lying on a bed of microneedles: An approach to isolate mechanical force. Proceedings of the National Academy of Sciences of the United States of America 100(4): 1484-1489.

6. Gray DS, Tien J, Chen CS (2003) Repositioning of cells by mechanotaxis on surfaces with micropatterned Young's modulus. Journal of Biomedical Materials Research Part A 66A(3): 605-614.

7. Zaari N, Rajagopalan P, Kim SK, Engler AJ, Wong JY (2004) Photopolymerization in microfluidic gradient generators: Microscale control of substrate compliance to manipulate cell response. Advanced Materials 16(23-24): 2133-2137.

8. Cukierman E, Pankov R, Stevens DR, Yamada KM (2001) Taking cell-matrix adhesions to the third dimension. Science 294(5547): 1708-1712.

9. Even-Ram S, Yamada KM (2005) Cell migration in 3D matrix. Current Opinion in Cell Biology 17(5): 524-532.

10. Zaman MH, Kamm RD, Matsudaira P, Lauffenburger DA (2005) Computational model for cell migration in three-dimensional matrices. Biophysical Journal 89(2): 1389-1397.

11. Berfield TA, Patel HK, Shimmin RG, Braun PV, Lambros J, Sottos NR (2006) Fluorescent image correlation for nanoscale deformation measurements. Small 2(5): 631-635.

12. Luo PF, Chao YJ, Sutton MA, Peters WH (1993) Accurate Measurement of 3-Dimensional Deformations in Deformable and Rigid Bodies Using Computer Vision. Experimental Mechanics 33(2): 123-132.

13. Vendroux G, Knauss WG (1998) Submicron deformation field measurements: Part 2. Improved digital image correlation. Experimental Mechanics 38(2): 86-92.

14. Sutton MA, Cheng MQ, Peters WH, Chao YJ, McNeill SR (1986) Application of an Optimized Digital Correlation Method to Planar Deformation Analysis. Image and Vision Computing 4(3): 143-150.

15. Bay BK, Smith TS, Fyhrie DP, Saad M (1999) Digital volume correlation: Three-dimensional strain mapping using X-ray tomography. Experimental Mechanics 39(3): 217-226.

16. Roeder BA, Kokini K, Robinson JP, Voytik-Harbin SL (2004) Local, three-dimensional strain measurements within largely deformed extracellular matrix constructs. Journal of Biomechanical Engineering-Transactions of the Asme 126(6): 699-708.

17. Smith TS, Bay BK, Rashid MM (2002) Digital volume correlation including rotational degrees of freedom during minimization. Experimental Mechanics 42(3): 272-278.

18. Corle TR, Kino GS (1996) Confocal scanning optical microscopy and related imaging systems. Academic Press. San Diego: xv, 335 p.

19. Sheppard C, Shotton D (1997) Confocal laser scanning microscopy. BIOS Scientific; Springer, in association with the Royal Microscopical Society. Oxford; New York: xii, 106 p.

20. Chen DJ, Chiang FP, Tan YS, Don HS (1993) Digital Speckle-Displacement Measurement Using a Complex Spectrum Method. Applied Optics 32(11): 1839-1849.

21. Takita K, Aoki T, Sasaki Y, Higuchi T, Kobayashi K (2003) High-accuracy subpixel image registration based on phase-only correlation. Ieice Transactions on Fundamentals of Electronics Communications and Computer Sciences E86A(8): 1925-1934.

22. Hong S, Ravichandran G (2006) FFT-based digital image correlation algorithm for large deformation measurements. in preparation.

23. Born M, Wolf E (1970) Principles of optics; electromagnetic theory of propagation, interference and diffraction of light. (4th ed). Pergamon Press. Oxford, New York: xxviii, 808p.

24. Gu M (1996) Principles of three dimensional imaging in confocal microscopes. World Scientific. Singapore ; River Edge, NJ: xii, 337 p.

25. Lucy LB (1974) Iterative Technique for Rectification of Observed Distributions. Astronomical Journal 79(6): 745-754.

26. Torok P, Varga P, Booker GR (1995) Electromagnetic Diffraction of Light Focused through a Planar Interface between Materials of Mismatched Refractive-Indexes - Structure of the Electromagnetic-Field .1. Journal of the Optical Society of America a-Optics Image Science and Vision 12(10): 2136-2144.

27. Sheppard CJR, Torok P (1997) Effects of specimen refractive index on confocal imaging. Journal of Microscopy-Oxford 185: 366-374.

28. Visser TD, Oud JL, Brakenhoff GJ (1992) Refractive-Index and Axial Distance Measurements in 3-D Microscopy. Optik 90(1): 17-19.

29. Diaspro A, Federici F, Robello M (2002) Influence of refractive-index mismatch in high-resolution three-dimensional confocal microscopy. Applied Optics 41(4): 685-690.

30. Ghahremani F (1980) Effect of Grain-Boundary Sliding on Anelasticity of Polycrystals. International Journal of Solids and Structures 16(9): 825-845.

31. Welsh ER, Tirrell DA (2000) Engineering the extracellular matrix: A novel approach to polymeric biomaterials. I. Control of the physical properties of artificial protein matrices designed to support adhesion of vascular endothelial cells. Biomacromolecules 1(1): 23-30.

List of Tables

Table B-1. Standard deviation values for measured displacement and strain fields in the undeformed condition.

	Stationary	Translation
u_1 [voxel]	0.0605	0.1392
u_2 [voxel]	0.0541	0.1238
u_3 [voxel]	0.2106	0.6491
ε_{11} (%)	6.39×10^{-3}	4.18×10^{-2}
ε_{22} (%)	9.80×10^{-3}	4.96×10^{-2}
ε_{33} (%)	0.260	0.718

Table B-2. Mean and standard deviation values for measured strain fields under uniaxial compression.

	No stretch-correlation		Stretch-correlation	
	Mean	Standard deviation	Mean	Standard deviation
ε_{11} (%)	7.69×10^{-3}	7.07×10^{-2}	-3.55×10^{-2}	7.37×10^{-2}
ε_{22} (%)	1.14×10^{-2}	6.83×10^{-2}	7.75×10^{-2}	7.11×10^{-2}
ε_{33} (%)	-9.25	0.866	-9.34	0.392

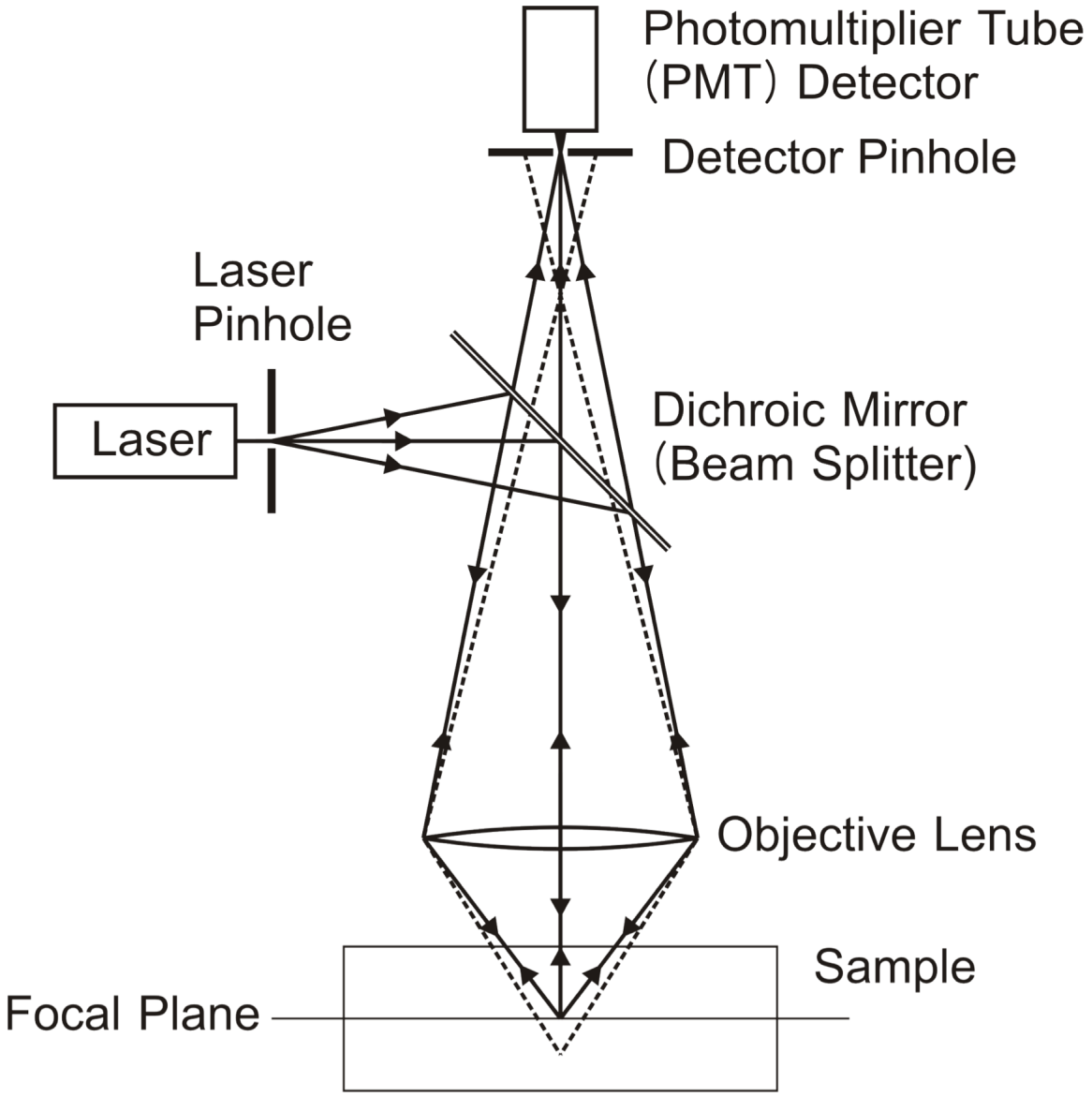

Figure B-1. Illustration of the confocal imaging principle
(solid lines = in-focus light; dashed lines = out-of-focus light)

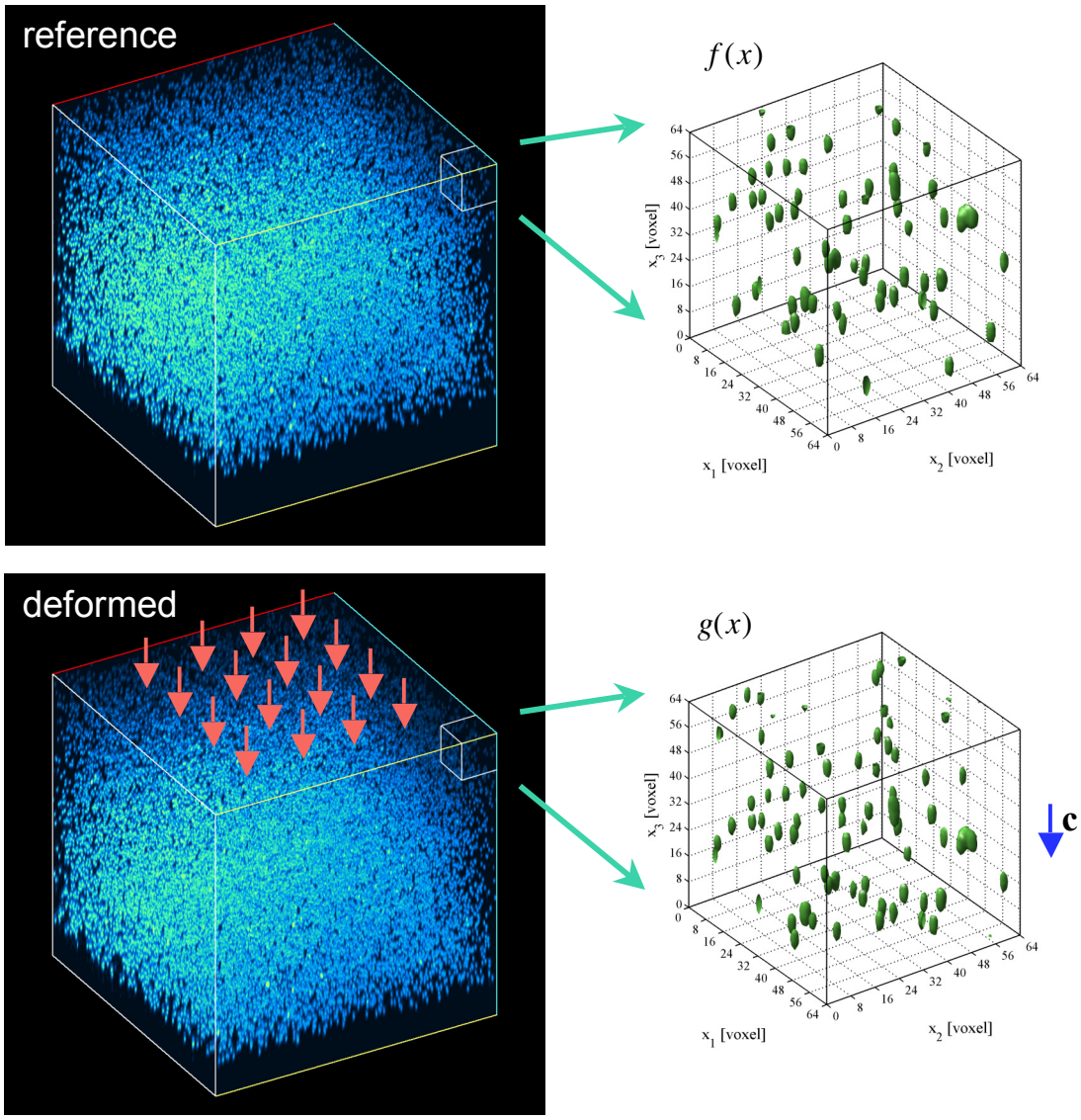

Figure B-2. Schematic illustration of the digital volume correlation (DVC)

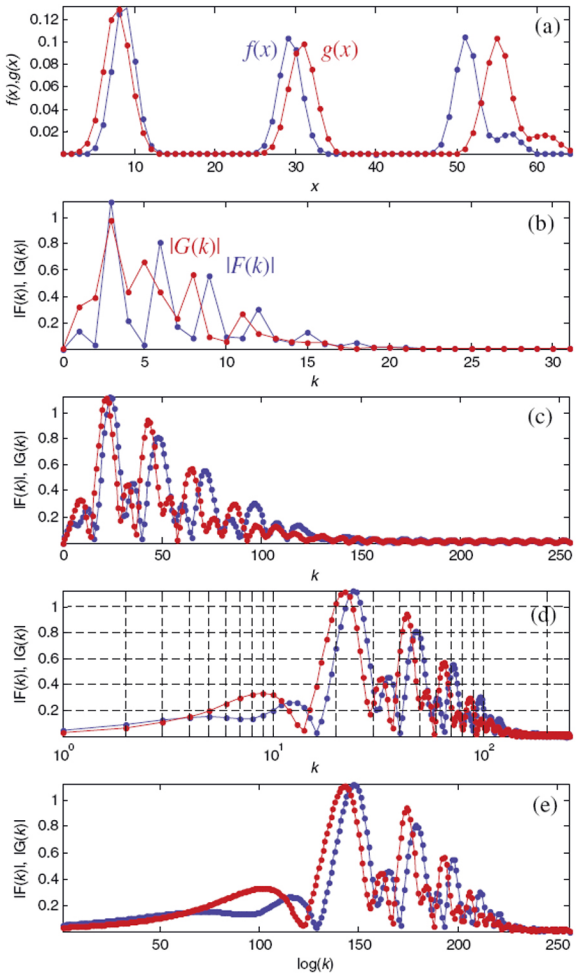

Figure B-3. One dimensional example of the stretch-correlation procedures

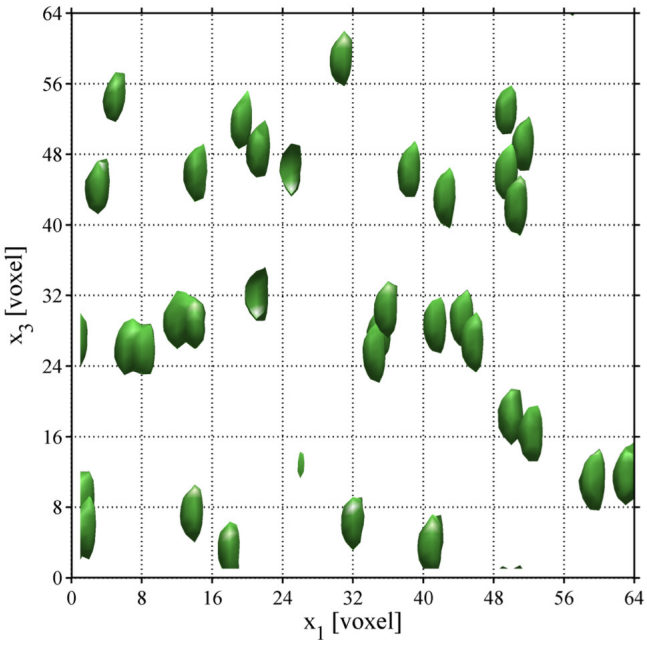

(a)

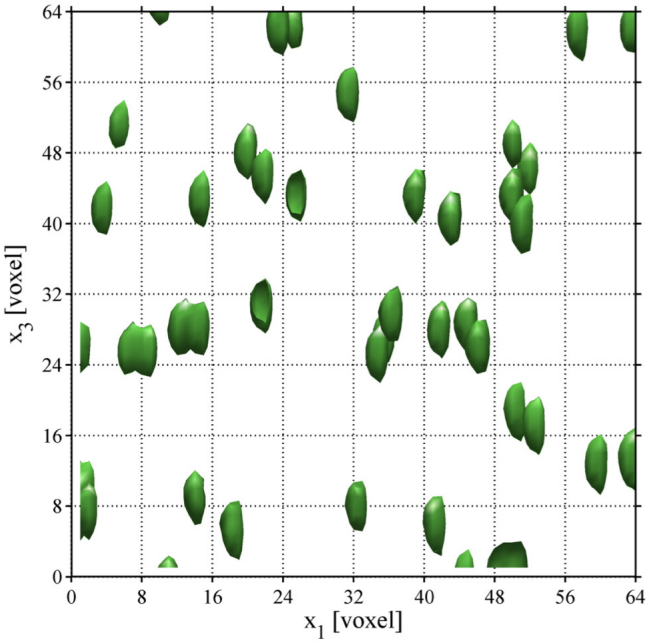

(b)

Figure B-4. 2-dimensional projection of confocal subvolume images (a) before and (b) after uniaxial compression of 10% in x_3-direction.

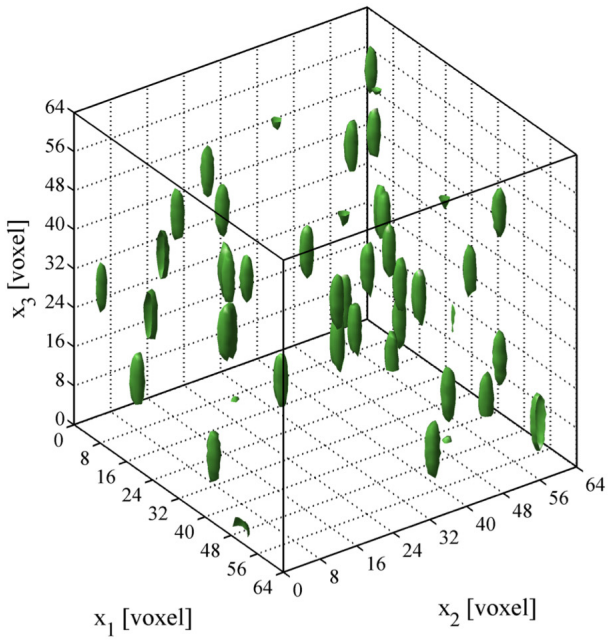

(a)

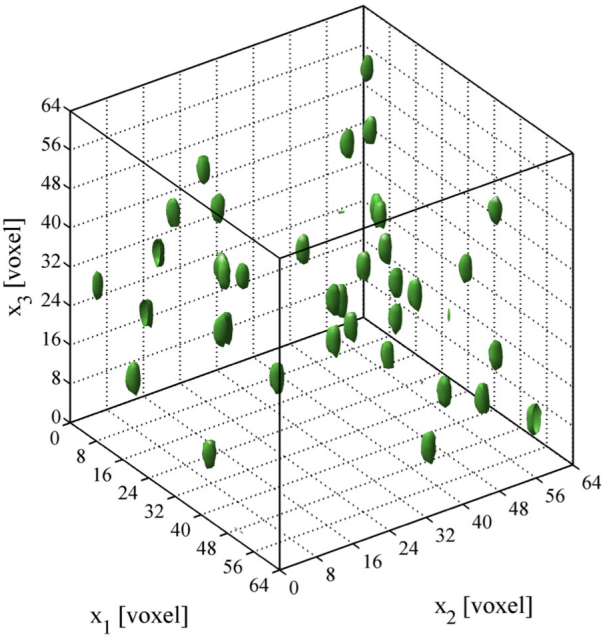

(b)

Figure B-5. Isosurface plots of confocal subvolume images
(a) before and (b) after deconvolution

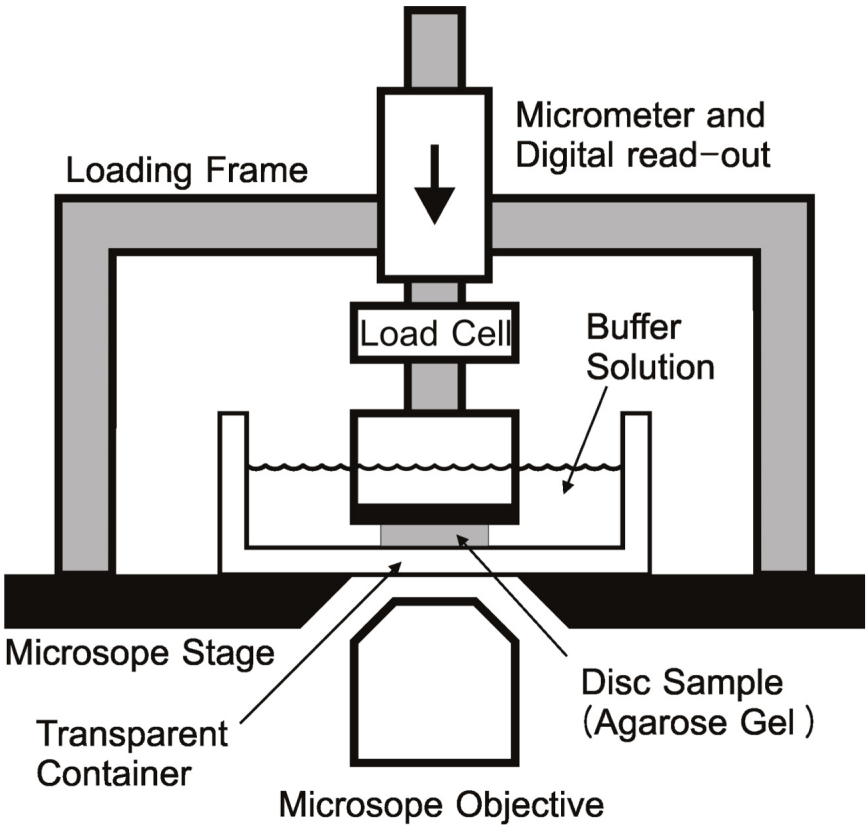

Figure B-6. Loading fixture for uniaxial compressive loading of soft materials

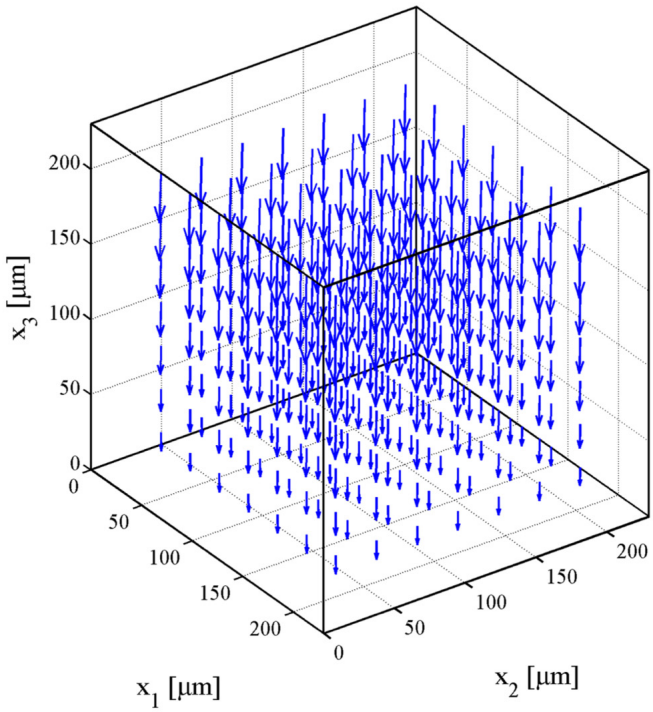

(a)

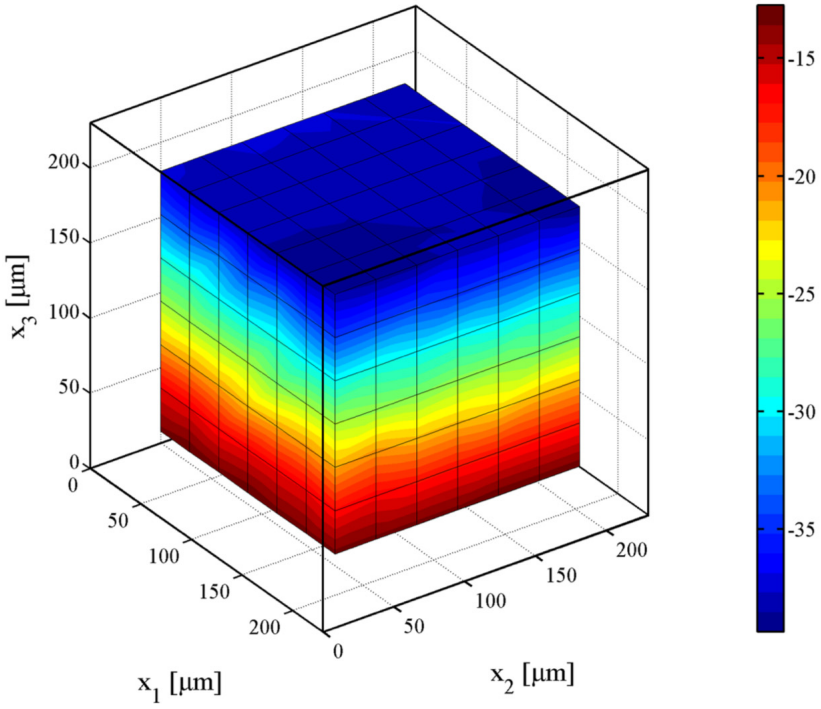

(b)

Figure B-7. Experimentally measured displacement fields under uniaxial compression (a) 3-dimensional displacement vector field and (b) vertical displacement field, u_3

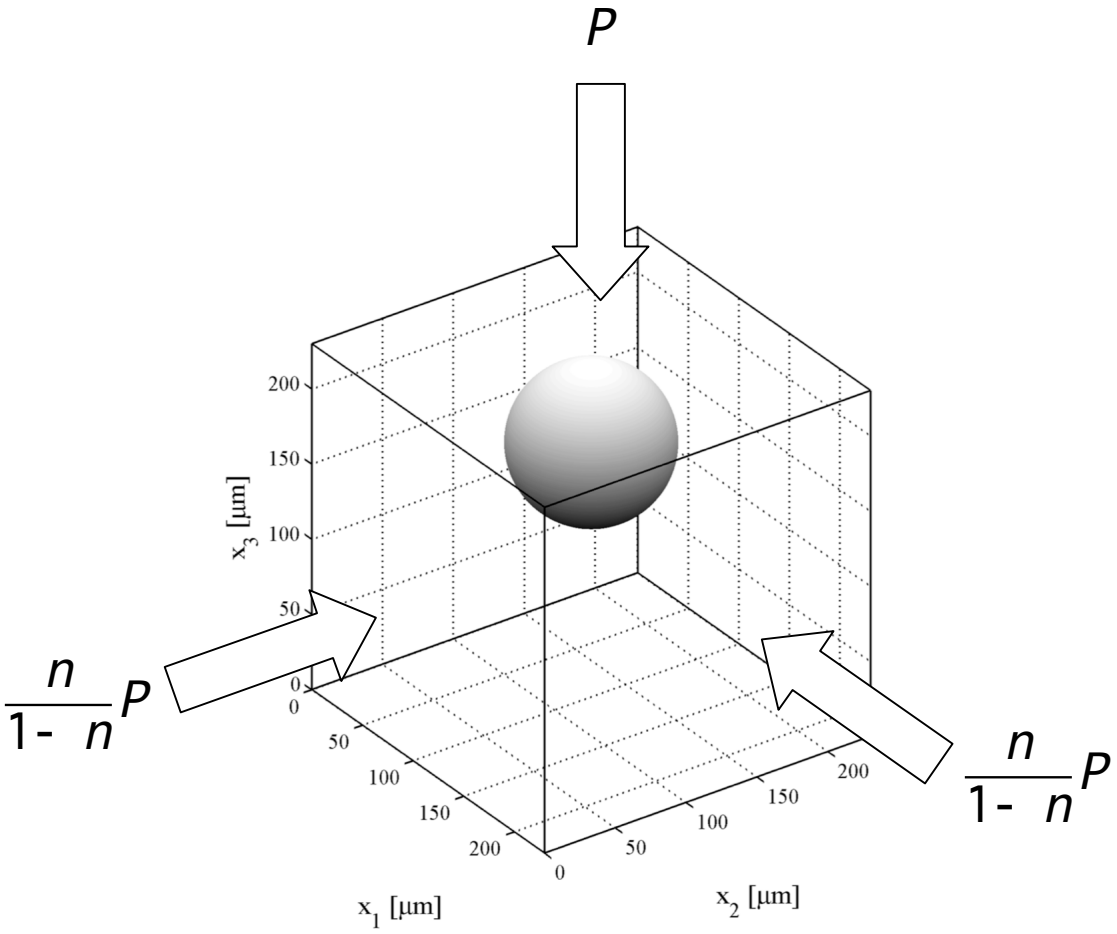

Figure B-8. Schematic of uniaxial constrained compression of a spherical inclusion in a matrix with a sliding interface

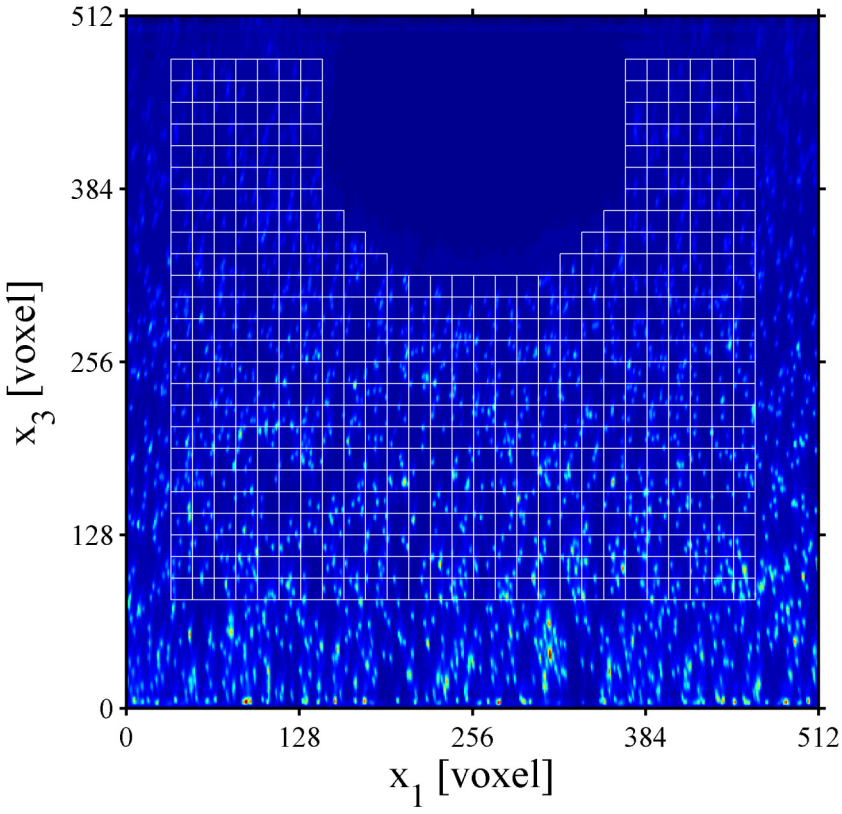

Figure B-9. A confocal slice along the meridian plane of an embedded 100 μm PMMA bead within the agarose sample

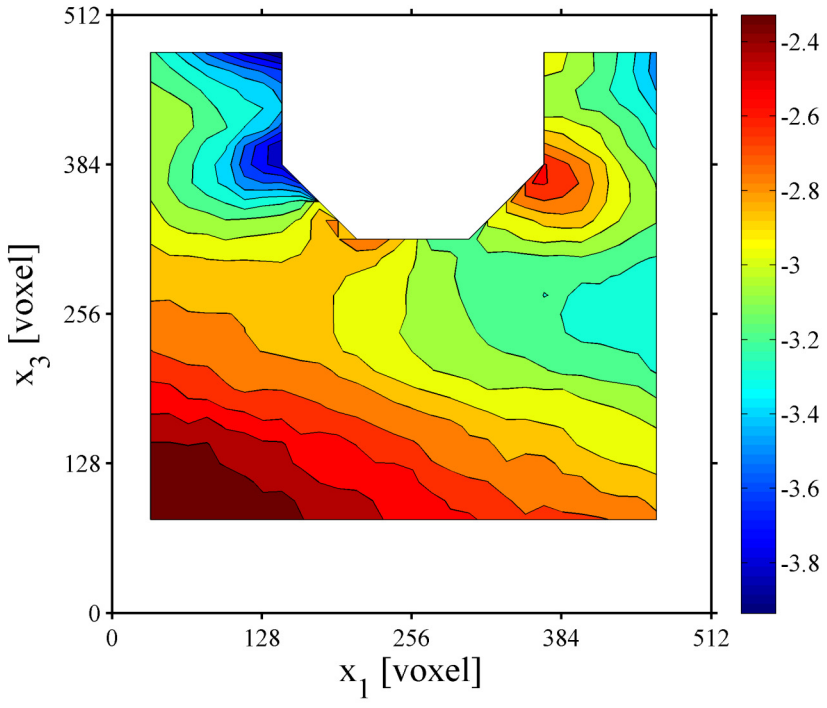

(a)

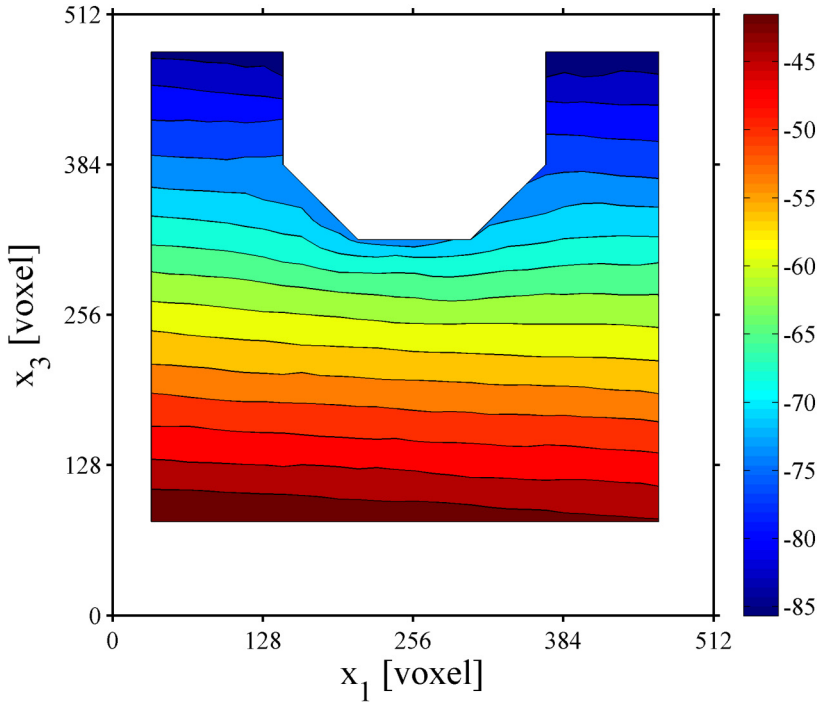

(b)

Figure B-10. Experimentally measured displacement fields near a spherical inclusion under uniaxial compression; (a) horizontal and (b) vertical displacement components

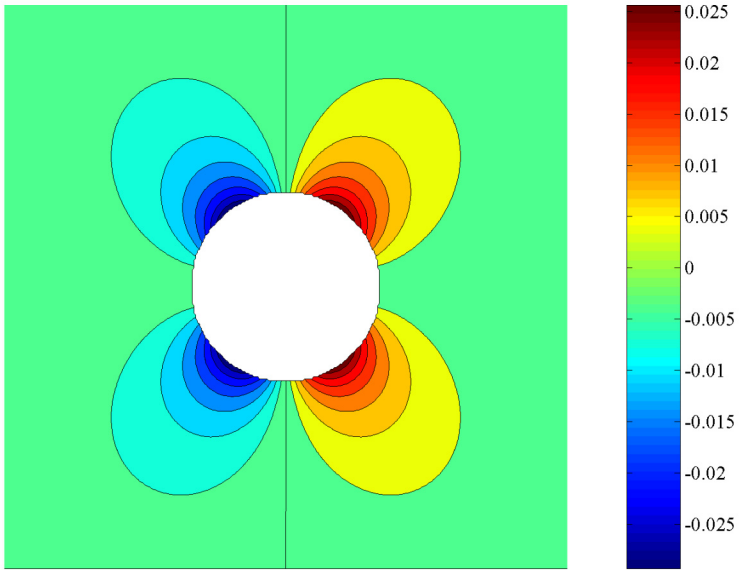

(a)

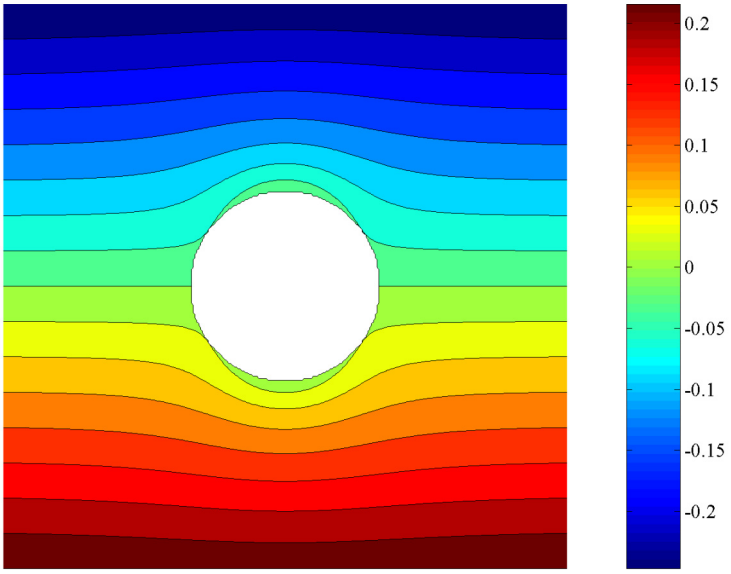

(b)

Figure B-11. Analytical displacement fields near a rigid inclusion with a sliding interface under uniaxial constrained compression; (a) horizontal and (b) vertical displacement components

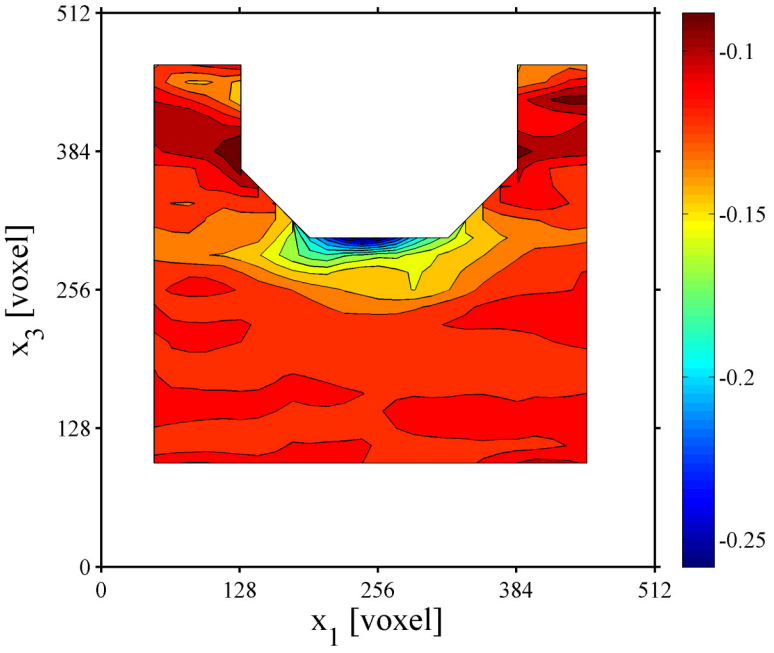

(a)

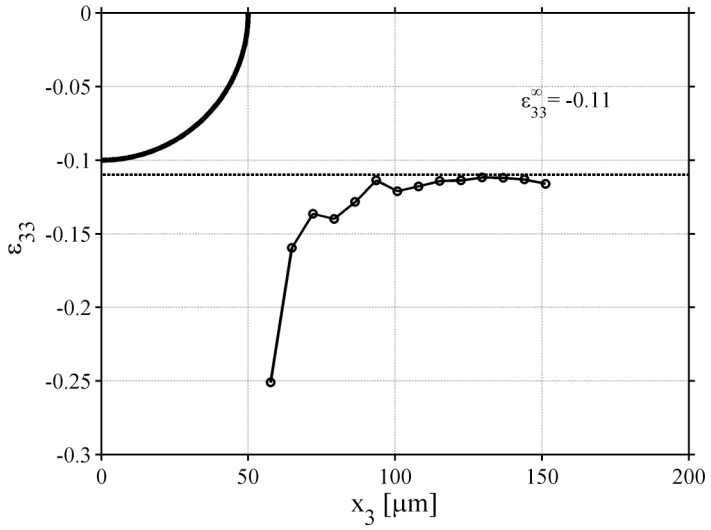

(b)

Figure B-12. Experimentally measured strain fields ε_{33} near a spherical inclusion under uniaxial compression.